Laser and Particle Beams (2010), *28*, 451–461.
© Cambridge University Press, 2010 0263-0346/10 $20.00
doi:10.1017/S0263034610000467

The TARANIS laser: A multi-Terawatt system for laser-plasma investigations

T. DZELZAINIS, G. NERSISYAN, D. RILEY, L. ROMAGNANI, H. AHMED, A. BIGONGIARI,
M. BORGHESI, D. DORIA, B. DROMEY, M. MAKITA, S. WHITE, S. KAR, D. MARLOW,
B. RAMAKRISHNA, G. SARRI, M. ZAKA-UL-ISLAM, M. ZEPF, AND C.L.S. LEWIS
School of Mathematics and Physics, Queen's University Belfast, Belfast, United Kingdom

(RECEIVED 30 May 2010; ACCEPTED 17 June 2010)

Abstract

The multi-Terawatt laser system, terawatt apparatus for relativistic and nonlinear interdisciplinary science, has been recently installed in the Centre for Plasma Physics at the Queen's University of Belfast. The system will support a wide ranging science program, which will include laser-driven particle acceleration, X-ray lasers, and high energy density physics experiments. Here we present an overview of the laser system as well as the results of preliminary investigations on ion acceleration and X-ray lasers, mainly carried out as performance tests for the new apparatus. We also discuss some possible experiments that exploit the flexibility of the system in delivering pump-probe capability.

Keywords: Laser; Plasma; Proton acceleration; X-ray lasers

1. INTRODUCTION

The multi-Terawatt chirped-amplification laser system, terawatt apparatus for relativistic and nonlinear interdisciplinary science (TARANIS), installed in the Centre for Plasma Physics at the Queen's University of Belfast is now operational, and preliminary investigations on laser-driven ion acceleration from solid targets and laser-pumped X-ray lasers have been carried out as performance tests for the system. This unique hybrid Ti:Sapphire-Nd:glass laser can simultaneously deliver two 1053 nm beams in each of the two existing target areas, in different combinations of ~700 fs/1 ns pulse and with intensities up to 10^{19} W/cm^2 in the short pulse mode and up to 30 J on target in the ns pulse mode. The TARANIS laser, along with a home-built synchronized femtosecond Ti:Sapphire laser will be used in the research areas of laser-field accelerated ion generation, warm dense matter, pump-probe experiments, and X-ray lasers. Due to its high degree of flexibility TARANIS should provide an excellent tool for original scientific research as well as bench-mark investigations carried out in support of work carried out at larger external high-power laser facilities such as PALS, VULCAN, NHELIX, and others (Zvorykin *et al.*, 2007; Jungwirth, 2005; Danson *et al.*, 2005; Neumayer *et al.*, 2005; Schaumann *et al*. 2005).

2. THE TARANIS LASER

A layout of the laser is shown in schematic form in Figure 1. The TARANIS laser is a hybrid Ti:Sapphire-Nd:glass system operating in the chirped pulse amplification mode. The laser front-end consists of a Ti:Sapphire oscillator, followed by a folded all-reflective stretcher, and by a Ti:Sapphire regenerative amplifier (RA). The oscillator, a commercial mode-locked system (Coherent Mira), provides a train of transform-limited, 120 fs long pulses at a wavelength of 1053 nm, with a repetition frequency of 76 MHz. The wavelength is chosen to match the peak of the Nd-Glass amplifiers gain curve in the glass amplification chain (see below), and, although the gain of the Ti:Sapphire crystal is not peaked at 1053 nm, the oscillator delivers an average power of 400 mW. Pulse stretching is achieved within the double-pass stretcher, equipped with a 1740 lines/mm diffraction grating and an $f = 1524$ mm spherical mirror arranged in an inverting telescope configuration. The stretcher bandpass is chosen to be about four times the oscillator output bandwidth, and the stretching factor is about 10^4, providing at the output ~1.2 ns long optically chirped pulses. Pre-amplification of the laser pulse is obtained in the Ti:Sapphire RA, pumped by a

---

Address correspondence and reprint requests to: D. Riley, School of Mathematics and Physics, Queen's University Belfast, Belfast, BT7 1NN, United Kingdom. E-mail: d.riley@qub.ac.uk

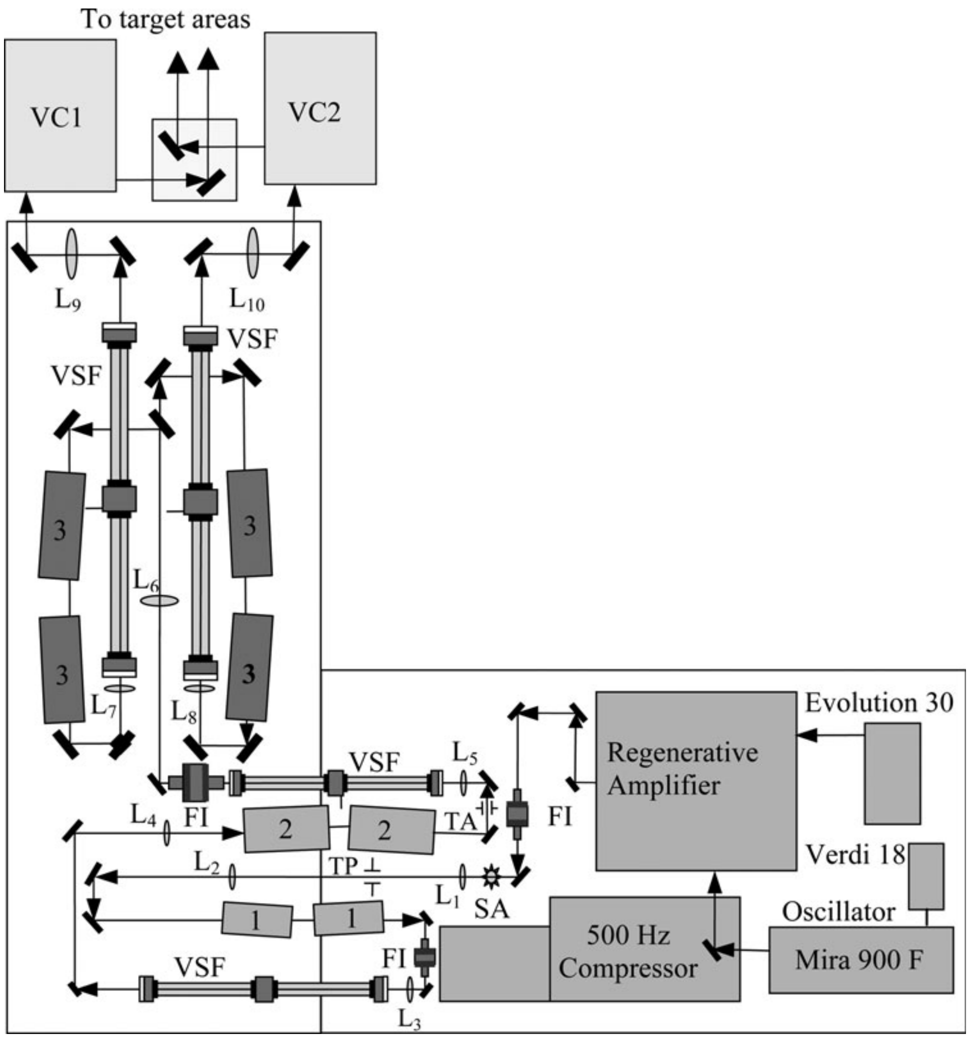

Fig. 1. Optical layout of TARANIS laser. FI – Faraday isolator; VSF – vacuum spatial filter; TA – Teflon aperture; TP – Teflon pinhole; SA – serrated aperture; 1, 2, 3 - laser heads with Nd:Glass rods of 9 mm, 25 mm, and 50 mm diameter, respectively; L_1L_2, L_3L_4, L_5L_6, L_7L_9, L_8L_{10} – relay imaging telescopes, VC1, VC2 – vacuum compressors.

commercial Q-switched Nd:YLF laser (Coherent Evolution) operating at the wavelength of 527 nm. The RA delivers ~0.6 mJ pulses (with an energy stability of ~3%) at a maximum frequency rate of 500 Hz in a ~300 mW average power beam. Optimization of the Ti:Sapphire RA for amplification at 1053 nm and a double set of Pockels cells located after the RA cavity contribute to limiting and controlling amplified spontaneous emission and pre-pulse activity.

Amplification to multi-TW levels is achieved within a three stage Nd:Glass amplification chain, optically pumped with flash lamps. The first two stages consist of phosphate-glass rods (each stage comprising two rods) of increasing diameter (length) of 9 mm (15 cm) and 25 mm (30 cm), respectively. The third stage consists of two parallel couples of rods (each rod being 50 mm in diameter and 30 cm in length) for amplification of two separate pulses up to peak energies of ~30 J per pulse at a repetition rate of 1 shot every 10 min in the full power mode. High spatial quality of the beam profile is ensured by relay-imaging in the vacuum spatial filters between the different amplification stages. In addition, the beam profile is spatially tailored by a 3.4 mm diameter serrated aperture, located at the input of the glass amplification chain and re-imaged through the system *via* the vacuum spatial filters. As a result of the tailoring and relay-imaging, the beam conserves a near-uniform top-hat spatial profile through the amplification chain, allowing optimal energy extraction from the glass rods. The two pulses from the glass amplification chain can be separately re-compressed in two double-pass grating compressors each one equipped with two 210 × 400 × 50 mm, 1740 lines/mm gold-coated diffraction gratings arranged in a parallel configuration. When a programmable acousto-optic modulator (Dazzler) is additionally employed in the laser chain in order to correct for high order phase distortions, a minimum pulse duration of 560 fs can be achieved, (700 fs is a typical average at high energy) with ~60% energy transmission through the compressors. A 30 J, ~1 ns long pulse can be obtained instead by optically bypassing the compressors. During experimental runs the pulse duration was monitored on a daily basis with an Angewandte Physik and Elektronik scanning autocorrelator, and in real time with a Coherent single shot autocorrelator. The pulse energy was also measured on each shot.

Several diagnostics have been installed to characterize and optimize the system performance. The diagnostics include real time energy, pre-pulse activity, and near/far field irradiance monitors as well as a single shot second-order autocorrelator all capable of operating on high power shots, while a scanning second-order autocorrelator with a frequency resolved optical gating option, and an optical spectrometer for spectral characterization of the laser pulse at different locations in the laser chain can be operated in the low-power, high repetition rate mode. The spectrometer can also be operated in single shot mode for monitoring of higher power shots.

In high-power, ultra-short laser pulse interactions with solid targets, short pre-pulses and the amplified spontaneous emission pedestal (pre-pulse activity) of the main laser pulse can create pre-ionization and expanding plasma before the main pulse arrival. This can distort the physical phenomena of the main interaction with solid targets. The reduction of pre-pulse activity in the TARANIS laser is performed by a pulse-picking technique using three Pockels cells installed within crossed polarizers. One Pockels cell before the regenerative amplifier and two others between the regenerative amplifier and the Nd:Glass amplifying chain are installed. The intensity contrast ratio is measured on a nanosecond timescale at low energy level of the laser output after compression of the regenerative amplifier pulses. The pre-pulse activity is recorded by a fast photodiode since it is more convenient for nanosecond time scales. Suitable optical filtering allows monitoring of the main laser pulse. The measured intensity contrast ratio is about 10^{-7}.

The architecture of the laser enables access to two different target areas, with a flexible choice of different long/short pulse combinations. A short pulse beam and an uncompressed, long pulse, beam can be simultaneously delivered to target area 1 (TA1), which has been designed mainly for investigations on X-ray lasers (e.g., see Kuroda *et al.*, 2005 and Baer *et al.*, 1996) and high energy density physics, while a combination of a short pulse and a long pulse or two short pulses can be delivered to target area 2 (TA2), which is mainly intended for experiments on laser-driven particle acceleration, X-ray sources, and applications. A 180 mJ pulse extracted after the 25 mm amplifiers and separately re-compressed down to 400 fs duration in a compact double diffraction grating compressor can be employed as a probe pulse for time-resolved optical probing measurements (optical interferometry, shadowgraphy or polarimetry) in either target areas.

3. PROTON ACCELERATION EXPERIMENTS WITH THE TARANIS LASER

The acceleration of proton beams (Snavely *et al.*, 2000; McKenna *et al.*, 2008) from laser-irradiated solid targets has been investigated employing the TARANIS laser system operating in the compressed pulse mode. The laser pulse from one of the main compressors was focused by employing an $f/3$, $f = 300$ mm off-axis parabola onto thin Aluminum foils of thicknesses ranging from 0.7 to 100 µm. The pulse before compression was ~10 J (of which ~7 J were delivered on target) in energy and ~560 fs in duration, and the focal spot diameter (measured in the low power, non amplified mode) was ~10 µm, leading to an intensity on target $\sim 2 \times 10^{19}$ Wcm^{-2}.

The proton beam emitted from the rear target surface (i.e., the non-irradiated surface) in the foil normal direction was detected employing multi-layer stacks of Gafchromic type HD-810 Radiochromic Films (RCFs). The RCF packs were wrapped in 11 µm aluminum foils in order to cut unwanted heavy ion and soft X-ray signals and to shield the pack from target debris, therefore giving minimum detectable proton energy of ~1 MeV. The multi-layer arrangement of the RCF stacks ensured a spectral multi-frame capability of the detection system. Protons with higher energies penetrate deeper in the stack and release their energy mainly in proximity of the Bragg peak. Each film in the stack acts as a filter for the following ones and spectrally selects the protons whose Bragg peak is localized within or in proximity of the active layer.

The RCF data was digitized employing a commercial optical scanner (Microtek ArtixScan 1800 f), with a maximum optical resolution of 1800 × 3600 dpi and a dynamic range nominally extending to optical densities up to 4.8. The scanning system was absolutely calibrated in dose employing a calibration target obtained by irradiating HD-810 RCFs with known proton doses from a particle accelerator. The single particle proton energy loss and stopping inside the RCF stack were modeled employing the Monte Carlo code SRIM. The response function (i.e., the energy deposited by a single proton *versus* the particle energy) of each RCF in a given stack was calculated from numerical integration of the stopping power curves obtained from SRIM simulations. This allowed the association of each film in the stack with a given proton energy range as well as the extraction of the absolute proton spectral density from the deposited dose in the film.

An example of typical RCF data obtained is shown in Figure 2 and typical spectra extracted from the data for different target thicknesses are shown in Figure 3. Typically the proton spectrum resembles a truncated Boltzmann-like distribution, with a temperature of 2.3 ± 0.1 MeV, with small variations depending on the target thickness (except that for 3 µm thick targets, which yield a temperature of 1.7 MeV), and with small shot to shot fluctuations. The dependence of the maximum proton energy and of the conversion efficiency as a function of the target thickness was investigated. A maximum proton energy of ~12 MeV was obtained for a target thickness of 10 µm (see Fig. 4), gradually decreasing when increasing the foil thickness. The gradual decrease in the maximum proton energy with increasing target thickness

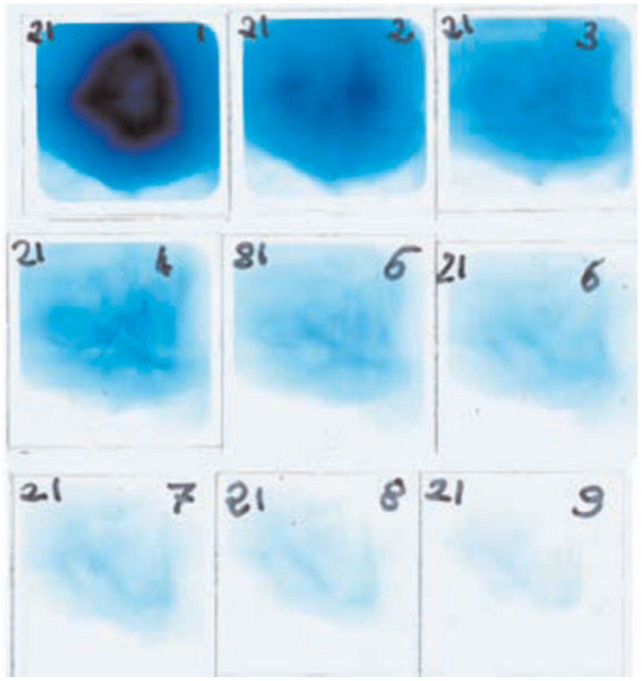

Fig. 2. (Color online) Typical RCF data with layers numbered (1–9) in sequence. Higher numbers correspond to higher energy protons with layer 1 corresponding to ~1 MeV and layer 9 to ~12 MeV. Each film subtended about 1 radian of arc with respect to the target.

can be explained in the frame of the target normal sheath acceleration model as a consequence of the decrease in the hot electron density due to a larger spatial spread of the electrons in the target (Fuchs *et al.*, 2006). The quick drop in the maximum energy for a target thickness below 6 μm on the other hand can be qualitatively explained as caused by the perturbation of the rear target side due to laser pre-pulse activity. Note that a detectable proton beam was accelerated for targets as thin as 1 μm, which is an indication of the high contrast level of the laser system. The maximum conversion efficiency from laser energy into accelerated particles was also obtained for 10 μm thick targets. The total number of particles accelerated in a single laser shot, obtained by integrating the proton spectrum from the minimum (~ 1 MeV) to the maximum (~ 12 MeV) detected proton energy, was in this case $\sim 3 \times 10^{11}$. This corresponds to a conversion efficiency from laser energy into total proton energy of ~2%, in agreement with results obtained from similar laser systems and with estimations from theoretical scaling laws (Borghesi *et al.*, 2008; Fuchs *et al.*, 2006).

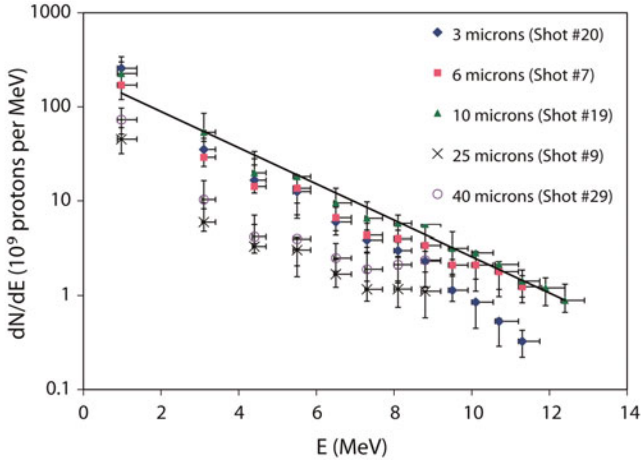

Fig. 3. (Color online) Typical proton spectra obtained for different target thicknesses.

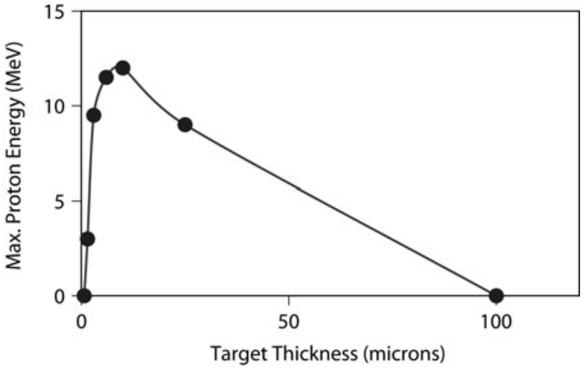

Fig. 4. Scan of maximum proton energy as a function of the target thickness.

4. X-RAY LASER EXPERIMENTS WITH THE TARANIS LASER

An investigation into the use of TARANIS as an X-ray laser (XRL) pump source has been made as a preliminary study with the ultimate aim of using the XRL as a dense plasma probe. The highly efficient grazing incidence pumping technique, first demonstrated by Keenan *et al.* (2005), has been chosen as the basic scheme due to the low powers required, which will leave a surplus of optical laser energy. In contrast to earlier transient collisional excitation schemes (King *et al.*, 2001), which used near normal incidence pulses with travelling wave techniques, the grazing incidence pumping scheme is characterized by the shallow grazing angle at which the main pump pulse is incident on the pre-formed plasma column. The shallow angle increases the coupling efficiency of the pump pulse into the gain region by first changing the turning point density to be at the optimum electron density for gain generation. Second, the path length of the pump pulse within the gain region is lengthened by the shallow angle and due to the fact that the pulse traverses the region twice.

4.1. Experimental Layout

A schematic diagram of the experimental layout for the XRL investigation is shown in Figure 5. The long pulse, shown in blue (color online only) entering from the upper right, was taken from the laser area before compression. It had an estimated pulse duration of ~1 ns and the energy used was

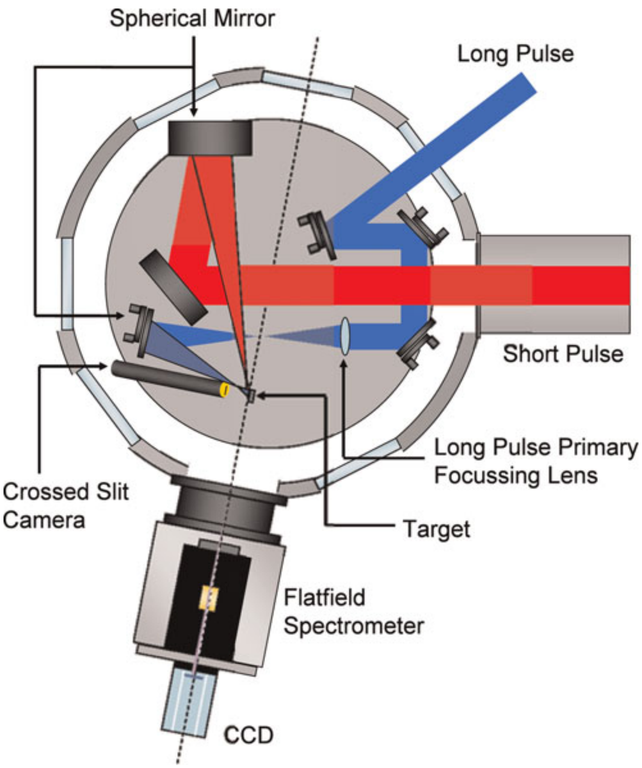

Fig. 5. (Color online) Schematic diagram of the experimental set-up used to investigate X-ray lasing on TARANIS.

typically 5–10 J. It was focused to a line of nominal length 9 mm and width 80 μm at near normal incidence by a combination of a $f = 300$ mm spherical lens, and a spherical mirror with a radius of curvature of 304.8 mm giving an intensity of between 5.8×10^{11} and 1.2×10^{12} Wcm^{-2}. The short pulse, shown in red (color online only) entering from the right, was compressed to between 600–800 fs. It was focused to a line of nominal length 7 mm and width 40 μm by a spherical mirror tilted at 10° to the incoming beam in accordance with the range used in other reported grazing incidence pulse schemes (Keenan *et al.*, 2005; Luther *et al.*, 2005; Kazamias *et al.*, 2008). The energy used was typically 2–5 J, giving an intensity of between 7.1×10^{14} and 1.8×10^{15} Wcm^{-2}. Prior to entering the chamber, the long pulse is directed through a variable delay line that allows the arrival of the long pulse to be varied from 4 ns ahead of short pulse to 1 ns after short pulse. The primary diagnostic is a flat-field spectrometer employing a variable spaced 1200 grooves/mm Hitachi grating coupled to a back thinned ANDOR CCD. To monitor plasma uniformity and line-focus overlap, a crossed-slit camera was installed below the experimental plane to observe the target surface at near normal incidence.

Line outs of an image from the crossed slit camera are shown for directions parallel and perpendicular to the XRL axis in Figures 6a and 6b, respectively. The intensity distributions are fitted with a Gaussian curves giving full width at half maximum values of 80 μm for width and 4.1 mm for length.

4.2. Results

Lasing from mid Z-number targets was investigated. Strong lasing was observed in Ni-like molybdenum on the 18.9 nm $4d_{3/2}$–$4p_{1/2}$ line and the 22.6 nm $4d_{3/2}$–$4p_{3/2}$ line. Strong lasing was also observed in Ni-like silver at 13.9 nm. Spectral line-outs of the molybdenum and silver XRLs are shown in Figures 7a and 7b, respectively. In each case the XRL line can be seen to have a large measured signal-to-noise ratio. It should be noted that the XRL linewidths are on the order of $\Delta\nu/\nu = 10^{-4}$ while the resolving power of the spectrometer is estimated at approximately 200–300. This means that the measured signal to noise ratio is limited by the spectral resolution of the spectrometer, and the true signal to noise value is expected to be more than an order of magnitude larger than that measured.

The delay between long pulse and short pulse was optimized by observing XRL output with varying long pulse-short pulse separation. It was found that the peak signal was seen with a delay of 1.0 ± 0.1 ns for Ni-like molybdenum, and 0.50 ± 0.1 ns for Ni-like silver. The difference

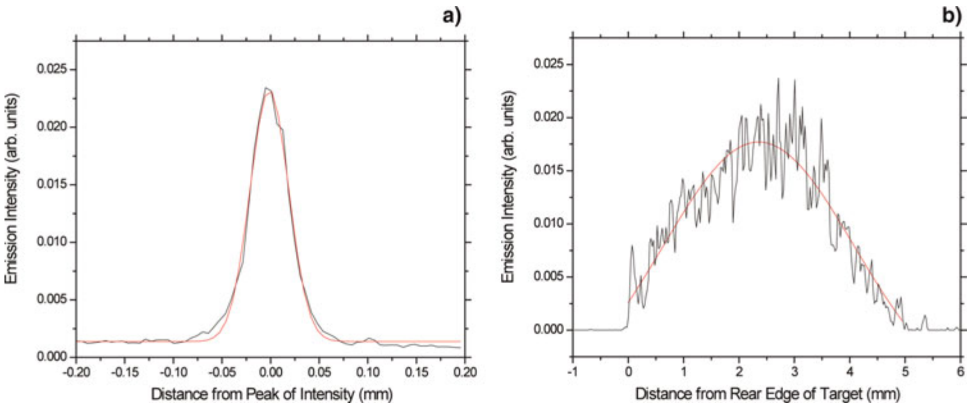

Fig. 6. (Color online) Emission intensity profiles (**a**) perpendicular and (**b**) parallel to the XRL axis.

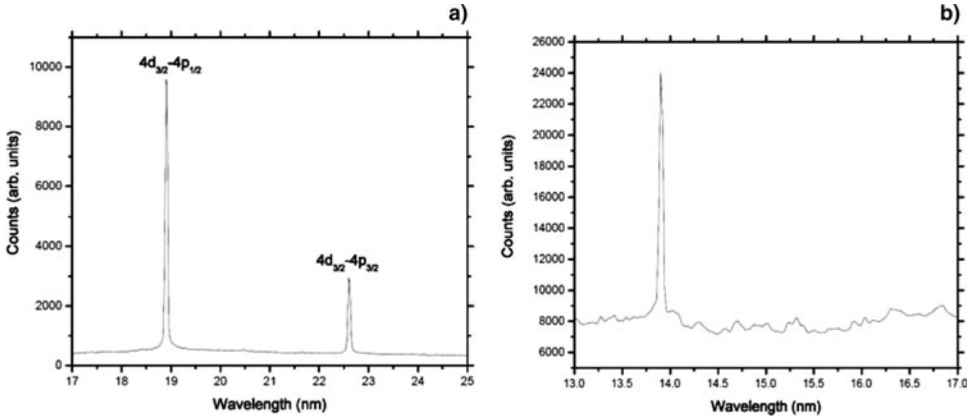

Fig. 7. Spectral line-outs for (**a**) Ni-like Mo and (**b**) Ni-like Ag XRLs.

in the optimum delay is explained by the fact that gold, being a higher Z-number element requires a hotter plasma to generate an abundant Ni-like population and that the XRL emission from Ni-like silver, at 13.9 nm it is able to propagate more efficiently through the high density gradients present at early times whereas the 18.9 nm and 22.9 nm emission from Ni-like molybdenum would suffer more severe refraction and be ejected from the gain region.

In order to check for saturation of the output, the XRL pulse energy was measured for varying target lengths. Growth curves for molybdenum and silver XRLs can be seen in Figures 8a and 8b, respectively. The Linford *et al.* (1974) approximation has been fitted to the data with the small signal gain coefficient determined by the first two experimental points. The "actual" gain coefficient as defined by Pert (1994) has been used. The value for the unsaturated small signal gain coefficient has been determined by fitting to the first two experimental data points. The Linford *et al.* (1974) approximation can be seen to over estimate the XRL output at the longest lengths by more than an order of magnitude.

It is believed that the discrepancy between the Linford *et al.* (1974) approximation and the experimental data is due to a non-uniform gain profile. There are several mechanisms that are expected to be present in the current experiment with the potential to lead to a non-uniform gain profile. First, non-uniform heating of the plasma column by a non-uniform line focus will produce non-uniform plasma conditions; such non-uniformity is evident from the emission profile shown in Figure 6b. Second, the grazing incidence pulse focusing geometry used in this experiment incorporates an inherent traveling wave pump. Simple ray-tracing can be used to show that the expected traveling wave speed is ~1.06c. The expected group velocity of the XRL pulse in the plasma is typically 0.85–0.95c. This means that the pump-pulse will, to some degree, "out-run" the XRL pulse, resulting in a delay between the pumping of the plasma and the arrival of the XRL pulse. During this time some decay of the gain profile is expected, leading to an effectively non-uniform gain profile that decreases toward the output edge of the target. Third, the refraction of the XRL pulse in the plasma acts to direct rays initially traveling parallel to the target surface into areas of lower electron density and hence lower gain, this means that even for an ideal, uniform gain region, the effective gain profile as seen by the XRL pulse will be one that decreases as the pulse propagates down the plasma column.

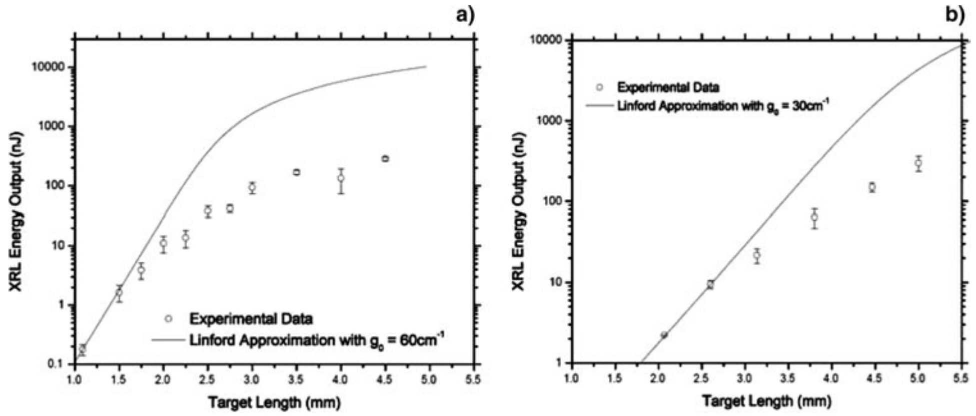

Fig. 8. Experimental growth curves for (**a**) Ni-like Mo and (**b**) Ni-like Ag XRLs fitted with the Linford approximation.

The fourth factor follows from the geometry of the focusing optic for the heating pulse. The large beam diameter of TARANIS, coupled with the relatively small target chamber, necessitate the use of a small F-number optic, leading to a large spread in angles of the rays arriving at different parts of the line focus. The central ray of the beam is incident at 20° grazing incidence, while those striking the rear edge of the target are incident at 22.3°, and those at the output edge are incident at 17.3°. The turning points of those rays near the rear edge of the target are then at higher electron densities than those at the output edge by a factor of 1.7. The gain is proportional to N_e^2, resulting in a gain that is expected to reduce by a factor of 2.9 from the rear edge to the output edge in a relatively linear fashion. The decay of the gain along the line focus is likely to be accentuated by the reduced inverse bremsstrahlung absorption at lower electron densities, which also varies according to N_e^2. As the velocity mismatch between the traveling wave and the XRL results in a temporal mismatch that is relatively small compared to the expected gain life-time, and the refraction expected within the 5 mm target length is not expected to be large enough to eject the XRL pulse from the gain region, it is thought that the line focus intensity profile and the spread in pump ray angles due to the geometry of the focusing optic would be the dominant factors in defining the gain profile. With all these effects combined, the gain could be reduced at the output edge to only a fraction of the value at the rear edge.

A generalized Linford *et al.* (1974) approximation has been formulated by Tommasini and Fill (2000) that can be used to calculated growth curves for arbitrary gain profiles. This has been used to investigate the shape of growth curves expected from gain profiles relevant to the current experiment in the absence of strong saturation effects. The profiles investigated and the corresponding growth curves are presented in Figures 9a and 9b, respectively. Although the curves can not be directly compared to the experimental data due to a lack of knowledge of the real gain profile, it can be concluded that saturation-like behavior can be induced in the measured growth curve of an XRL even when strong saturation is not present, such behavior could also cause a weakly saturated laser to appear deeply saturated, especially where output energy levels are not known in absolute units.

5. FUTURE EXPERIMENTS WITH TARANIS

As can be seen from the preceding sections, TARANIS is a versatile laser capable of generating high quality scientific data. Future plans for the laser are wide ranging. In this section, we outline just a sample of future plans that make full use of the laser's capabilities in XRL and proton beam production.

5.1. Collisional Absorption of X-ray-ultraviolet Radiation in Warm Dense Matter

The study of warm dense matter is a growing scientific activity (Lee *et al.*, 2002). This is because of its strong relevance to inertial confinement fusion, where both pusher and fuel pass through the warm dense matter regime during the compression and the planetary interiors, which are believed to be in a warm dense matter state (Drake, 2009; National Research Council, 2003). There are many possible experiments that probe the properties of warm dense matter. In the following, we outline an experiment that measures the collisional absorption of X-ray-ultraviolet radiation of solid density matter at temperatures of ~1 eV. For this temperature range, we can see (Eidmann *et al.*, 2000; Semkat *et al.*, 2006) that the effective electron-ion collision model of the solid is intermediate between the plasma (Spitzer) case where the scaling is $\nu_{ei} \sim T_e^{-3/2}$ and solid state, electron-phonon models where $\nu_{eI\text{-phonon}} \sim T_i$. The effective cold collision frequency for aluminum is $\sim 8.5 \times 10^{14}\ s^{-1}$. As the Al heats to 1 eV this rises to over $10^{16}\ s^{-1}$. In Eidmann *et al.* (2000), a harmonic mean is used to interpolate between the regimes, giving a collision frequency that is less strongly dependent on temperature. Broadly, similar results are achieved with detailed calculations by Semkat *et al.* (2006). In their simulations, the ion-ion static structure

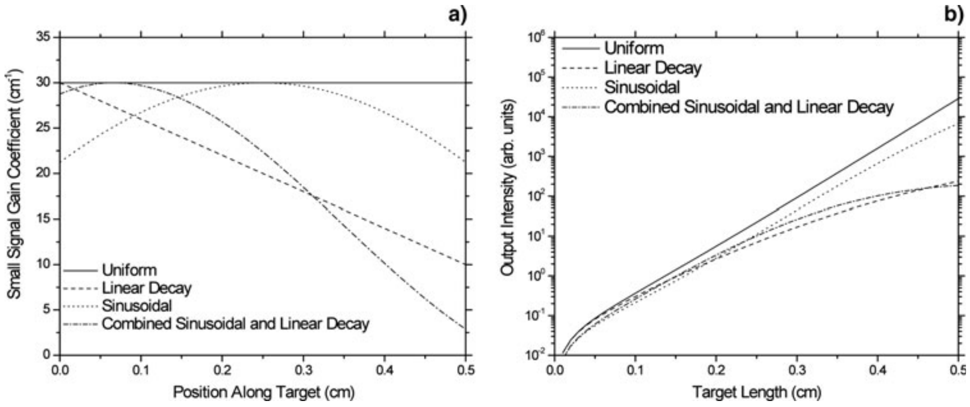

Fig. 9. (**a**) Possible gain profiles produced in the current experiment and (**b**) corresponding growth curves predicted by the "generalized Linford formula" of Tommasini and Fill (2000).

factor plays a role. They predict that for temperatures below ~10 eV we should see a relatively constant value of $\nu_{\mathrm{ei}}(\omega)$. This means that we can usefully probe this value experimentally with modest accuracy in our knowledge of the temperature. This would thus provide a useful experimental test of theory in a regime of current interest.

We can carry out a relevant experiment at TARANIS with its dual beam capability. We need only 5 J in long pulse and short pulse to generate an XRL at 18.9 nm as described above. By splitting beams we will still be capable of delivering ~15 J in 1 ps to create a proton beam. This proton beam can be used to create a warm dense matter sample (Patel *et al.*, 2003; Roth *et al.*, 2009).

In Figure 10, we show how such an experiment could be laid out. The integrated target structure required is shown in schematic form, for clarity. The divergence of the XRL is ~15 mrad and so if it is placed ~10 cm from the sample foil it will subtend ~1.5 mm. By making the sample foil into a narrow strip of ~0.5–1 mm width we will be able to observe the XRL as is passes both through and past the sample, giving a clear measure of transmission in a regime of interest to warm dense matter physics.

The proton beam is generated by irradiation of a secondary metal foil. This can generate a total of $\sim 10^{12}$ protons with a beam "temperature" of ~2 MeV and a beam divergence of ~0.5 radians. In fact, as described above, our own data on TARANIS has measured protons between 1–12 MeV with a distribution given by:

$$\frac{dN}{dE} \approx 2.15\times10^{11}e^{-0.44E} \quad \mathrm{MeV}^{-1}$$

for ~7 J on target. The sample foil in the experiment would be very thin to allow a reasonable value of opacity. For example, we can obtain 0.8 μm thick aluminum commercially. The cold transmission of such a foil at 18.9 nm would be 32% (Henke *et al.*, 1993). This means the sample is about one absorption depth thick and the transmission is sensitive to changes in opacity as the target is heated and expands. For protons in aluminum, the stopping power is on the order of 200 MeV cm^2/g at ~1 MeV and drops at higher energy (ICRU, 1993). For low energy, the stopping rises to a maximum of ~500 MeV cm^2/g. In Figure 11, we show the predicted energy deposition in a thick aluminum foil assuming a similar distribution as above but for ~10 J on target. We assume that we have the sample foil 0.5 mm from the proton generation foil and that the divergence of the proton beam is ~0.5 radians. As we can see, if we place a ~10 μm thick aluminum moderator foil before the sample, we can deposit >4 eV per atom quite uniformly through a 0.8 μm sample. This is more than sufficient to melt the solid into a warm dense matter state. The moderator foil also has the advantage that it will stop any heavy ions from reaching the sample. These would have a much stronger stopping power and might create a less uniform sample. Of course, with such a range in proton energies and a finite distance to the sample foil, the energy is deposited over a finite time. In Figure 12, we can see the temporal history of the deposition in a thin slice of the foil, buried 10 μm into the foil. We can simulate the effect of this heating by assuming all energy is deposited into electrons and inserting this profile as an electron heating term into the Hyades hydrodynamic code. We assume that we have a 10 μm thick moderator foil that slows the protons before they enter a 0.8 μm

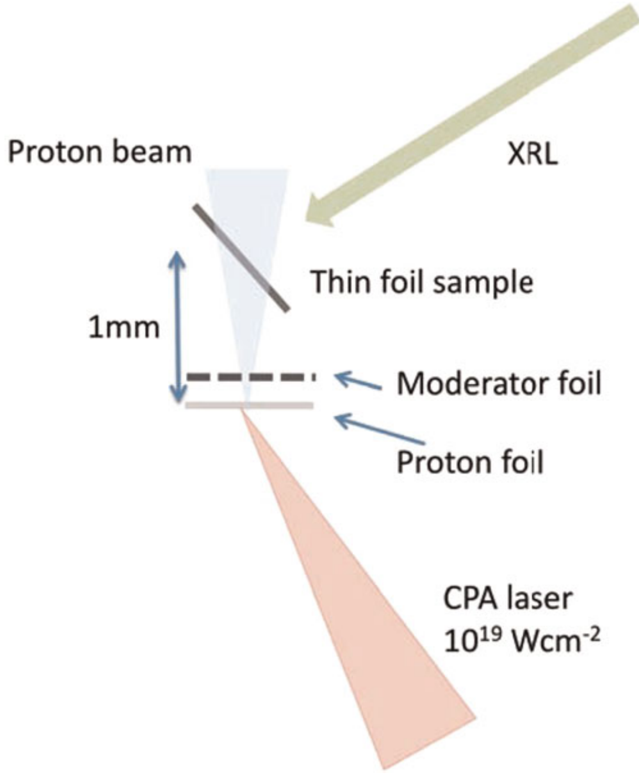

Fig. 10. (Color online) Schematic of possible opacity experiment on proton heated matter.

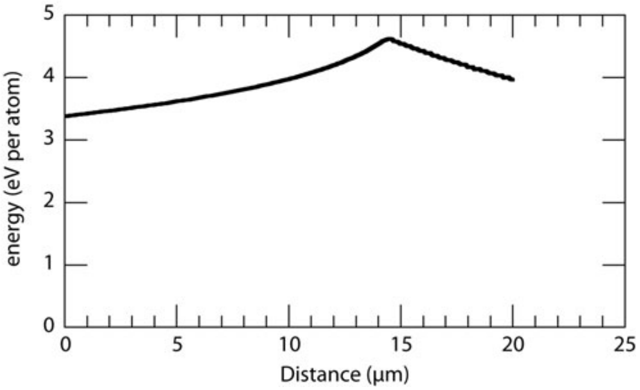

Fig. 11. Deposition of energy in an Al foil using our proton beam parameters from 1–12 MeV and the stopping powers from International Commission on Radiation Units and Measurements (1993). The cusp at ~15 microns corresponds to the Bragg peak of the slowest groups of protons at (~1 MeV).

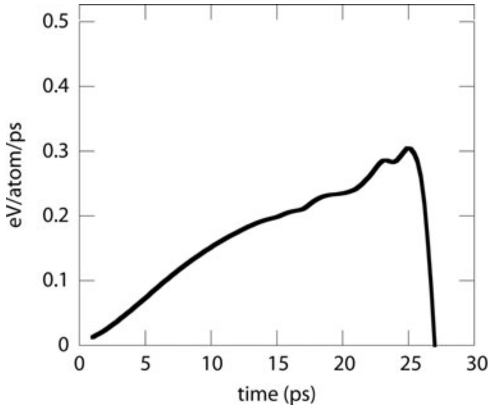

Fig. 12. Temporal evolution of proton heating pulse after 10 microns of Al.

aluminum foil where they deposit energy uniformly in space but with the temporal history of Figure 12.

In Figure 13, we see the profile of density and temperature at the end of the heating pulse of protons and note that the density has remained high, and the temperature has reached ~1.5 eV. The bulk of the proton beam energy will in fact pass through a thin foil and we can use an RCF stack to measure the energy in the proton beam. Since stopping powers have been quite carefully tabulated to within ~5% from experimental data, we will be in a position to accurately estimate the energy deposited on each shot. This will provide a benchmarking parameter for detailed hydrodynamic simulations comparing the effects of changing the equation of state/or ionization model on the hydrodynamic conditions and predicted opacity.

Since the L-shell is too deeply bound for photo-ionization with 66 eV photons, collisional absorption will be dominant for the solid density regime where the M-shell electrons are in a conduction band. As the density falls, we will see atomic aluminum appear and thus photo-ionization from the M-shell will play a role. The hydrodynamic simulations indicate that this will not happen until >50 ps after heating for the bulk of the foil, but the outer edges of the foil will fall more rapidly and a detailed simulation will be used to simulate transmission.

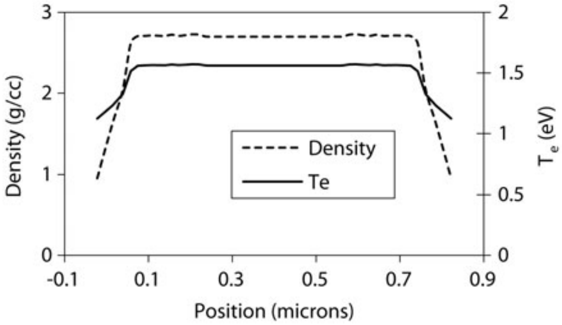

Fig. 13. Density and temperature of the sample foil at the end of the proton heating pulse.

5.2. Ablation and Warm Dense Matter Production with XRL Radiation

One potential use of the TARANIS X-ray laser is in the investigation X-ray-ultraviolet interaction with solids. With the advent of new light sources such as the FLASH X-ray-ultraviolet free electron laser (Ackermann *et al.*, 2007) and the potential for moving lithographic techniques for microchip production to the X-ray-ultraviolet regime (Newman, 1991), this has become a topic of current interest, with measurements of transmission of X-ray-ultraviolet beams through thin foils (Nagler *et al.*, 2009) using the FLASH facility and ablation measurements of solids with similar X-ray lasers (Faenov *et al.*, 2009) having been already made. The high photon energy (89 eV in the gold XRL case and 66 eV for molybdenum) means that mechanisms of ablation and damage might be expected to be quite different to the optical case. By use of a multi-layer optic, we can expect to focus the beam to approximately 20 μm diameter. With energy of ~1 μJ possible at 18.9 nm in the molybdenum case, we can conservatively estimate 50% reflectivity of the pulse. The muti-layer mirrors have a broad reflectivity of about 10% bandwidth. We can use a Zr filter with ~40% transmission to reduce the effect of thermal emission from the laser-plasma used as the XRL medium. This means that we could potentially generate a fluence of >50 mJ/cm^2. This is well in excess of the ablation threshold found for LiF at similar wavelengths by Faenov *et al.* (2009) and means that we have the latitude to investigate a variety of materials with differing ablation thresholds.

If we choose our material carefully we can have a cold opacity of ~10^5 cm^2/g, for example, Fe at 18.9 nm. This means that the energy can be absorbed in a relatively thin layer (15 nm of Fe). This in turn means the energy per atom is ~5 eV. This is more than enough to melt the sample into a warm dense matter state. The advantage of such heating is that it is essentially volumetric and happens within the pico-second duration of the XRL. The subsequent expansion of the layer can be observed with techniques such as Fourier domain interferometry for comparison with simulations based on different equations of state.

6. SUMMARY

As we have seen in the preceding sections, the TARANIS laser is a powerful and versatile tool with which we can carry out a range of experiments. The preceding section outlines just a small part of the potential scientific program. In addition to the generation of X-ray lasers and energetic particle beams, it can also be used to drive megabar level shocks and generate high harmonics in the X-ray-ultraviolet regime.

ACKNOWLEDGMENTS

The authors are grateful for financial support from the UK Engineering and Sciences Research Council under grants EP/C003586/1, EP/G007462/1, EP/D06337X/1 and EP/E035728/1. We also thank S. Green and D. Kirby for calibration of the RCF.

REFERENCES

Ackermann, W., Asova, G., Ayvazyan, V., Azima, A., Baboi, N., Baehr, J., Balandin, V., Beutner, B., Brandt, A., Bolzmann, A., Brinkmann, R., Brovko, O.I., Castellano, M., Castro, P., Catani, L., Chiadroni, E., Choroba, S., Cianchi, A., Costello, J.T., Cubaynes, D., Dardis, J., Decking, W., Delsim-Hashemi, H., Delserieys, A., Di Pirro, G., Dohlus, M., Duesterer, S., Eckhardt, A., Edwards, H.T., Faatz, B., Feldhaus, J., Floettmann, K., Frisch, J., Froehlich, L., Garvey, T., Gensch, U., Gerth, Ch., Goerler, M., Golubeva, N., Grabosch, H.-J., Grecki, M., Grimm, O., Hacker, K., Hahn, U., Han, J.H., Honkavaara, K., Hott, T., Huening, M., Ivanisenko, Y., Jaeschke, E., Jalmuzna, W., Jezynski, T., Kammering, R., Katalev, V., Kavanagh, K., Kennedy, E.T., Khodyachykh, S., Klose, K., Kocharyan, V., Koerfer, M., Kollewe, M., Koprek, W., Korepanov, S., Kostin, D., Krassilnikov, M., Kube, G., Kuhlmann, M., Lewis, C.L.S., Lilje, L., Limberg, T., Lipka, D., Loehl, F., Luna, H., Luong, M., Martins, M., Meyer, M., Michelato, P., Miltchev, V., Moeller, W.D., Monaco, L., Mueller, W.F.O., Napieralski, O., Napoly, O., Nicolosi, P., Noelle, D., Nunez, T., Oppelt, A., Pagani, C., Paparella, R., Pchalek, N., Pedregosa-Gutierrez, J., Petersen, B., Petrosyan, B., Petrosyan, G., Petrosyan, L., Pflueger, J., Ploenjes, E., Poletto, L., Pozniak, K., Prat, E., Proch, D., Pucyk, P., Radcliffe, P., Redlin, H., Rehlich, K., Richter, M., Roehrs, M., Roensch, J., Romaniuk, R., Ross, M., Rossbach, J., Rybnikov, V., Sachwitz, M., Saldin, E.L., Sandner, W., Schlarb, H., Schmidt, B., Schmitz, M., Schmueser, P., Schneider, J.R., Schneidmiller, E.A., Schnepp, S., Schreiber, S., Seidel, M., Sertore, D., Shabunov, A.V., Simon, C., Simrock, S., Sombrowski, E., Sorokin, A.A., Spanknebel, P., Spesyvtsev, R., Staykov, L., Steffen, B., Stephan, F., Stulle, F., Thom, H., Tiedtke, K., Tischer, M., Toleikis, S., Treusch, R., Trines, D., Tsakov, I., Vogel, E., Weiland, T., Weise, H., Wellhoeffer, M., Wendt, M., Will, I., Winter, A., Wittenburg, K., Wurth, W., Yeates, P., Yurkov, M.V., Zagorodnov, I., Zapfe, K. (2007). Operation of a free-electron laser from the extreme ultraviolet to the water window *Nat. Photonics* **1**, 336–342.

Baer, A., Eliezer, S., Henis, Z., Schwob, J.L. (1996). X-ray laser scheme driven by two laser pulses. *Laser Part. Beams* **14**, 625–630.

Borghesi, M., Bigongiari, A., Kar, S., Macchi, A., Romagnani, L., Audebert, P., Fuchs, J., Toncian, T., Willi, O., Bulanov, S.V., Mackinnon, A.J. & Gauthier, J.C. (2008). Laser-driven proton acceleration: Source optimization and radiographic applications. *Plasma Phys. Control. Fusion* **50**, 124040.

Danson, C.N., Brummitt, P.A., Clarke, R.J., Collier, I., Fell, B., Frackiewicz, A.J., Hawkes, S., Hernandez-Gomez, C., Holligan, P., Hutchinson, M.H.R., Kidd, A., Lester, W.J., Musgrave, I.O., Neely, D., Neville, D.R., Norreys, P.A., Pepler, D.A., Reason, C., Shaikh, W., Winstone, T.B., Wyatt, R.W.W. & Wyborn, B.E. (2005). Vulcan petawatt: Design, operation and interactions at 5×10^{20} Wcm^{-2}. *Laser Part. Beams* **23**, 87–93.

Drake, R.P. (2009). Perspectives on high-energy-density physics. *Phys. Plasmas* **16**, 055501.

Eidmann, K., Meyer-ter-Vehn, J., Schlegel, T. & Hüller S. (2000). Hydrodynamic simulation of subpicosecond laser interaction with solid-density matter. *Phys. Rev. E* **62**, 1202–1214.

Faenov, A.Ya, Inogamov, N.A.,Zhakhovskii, V.V., Khokhlov, V.A., Nishihara, K., Kato, Y., Tanaka, M., Pikuz, T.A., Kishimoto, M., Ishino, M., Nishikino, M., Nakamura, T., Fukuda, Y., Bulanov, S.V. & Kawachi, T. (2009). Low-threshold ablation of dielectrics irradiated by picosecond soft X-ray laser pulses. *Appl. Phys. Lett.* **94**, 231107.

Fuchs, J., Antici, P., D'Humieres, E., Lefebvre, E., Borghesi, M., Brambrink, E., Cecchetti, C.A., Kaluza, M., Malka, V., Manclossi, M., Meyroneinc, S., Mora, P., Schreiber, J., Toncian, T., Pepin, H. & Audebert, P. (2006). Laser-driven proton scaling laws and new paths towards energy increase, *Nat. Phys.* **2**, 48–54.

Henke, B.L., Gullikson, E.M. & Davis, J.C. (1993). X-ray Interactions-Photoabsorption, Scattering, Transmission and Reflection at E = 50–30,000 eV, Z = 1–92. *Atomic Data and Nuclear Data Tables* **54**, 181–342.

International Commission on Radiation Units and Measurements. (1993). Stopping Powers and Ranges for Protons and Alpha Particles. ICRU Report 49.

Jungwirth, K. (2005). Recent highlights of the PALS research program. *Laser Part. Beams* **23**, 177–182.

Kazamias, S., Cassou, K., Ros, D., Plé, F., Jamelot, G., Klisnick, A., Lundh, O., Lindau, F., Persson, A., Wahlström, C.-G., De Rossi, S., Joyeux, D., Zielbauer, B., Ursescu, D. & Kühl, T. (2008). Characterization of a transient collisional Ni-like molybdenum soft-X-ray laser pumped in grazing incidence. *Phys. Rev. A* **77**, 033812.

Keenan, R., Dunn, J., Patel, P.K., Price, D.F., Smith, R.F. & Shlyapstev, V.N. (2005). High-repetition-rate grazing-incidence pumped X-ray laser operating at 18.9 nm. *Phys. Rev. Lett.* **94**, 103901.

King, R.E., Pert, G.J., McCabe, S.P., Simms, P., MacPhee, A.G., Lewis, C.L.S., Keenan, R., O'Rourke, R.M.N., Tallents, G.J., Pestehe, S.J., Strati, F., Neely, D. & Allot, R. (2001). Saturated X-ray lasers at 196Å and 73Å pumped by picosecond, travelling wave excitation. *Phys. Rev. A* **64**, 053810/1–12.

Kuroda, H., Suzuki, M., Ganeev, R., Zhang, J., Baba, M., Ozaki, T., Wei, Z.Y. & Zhang, H. (2005). Advanced 20 TW Ti:S laser system for X-ray laser and coherent XUV generation irradiated by ultra-high intensities. *Laser Part. Beams* **23**, 183–186.

Lee, R.W., Baldis, H.A., Cauble, R.C., Landen, O.L., Wark, J.S., Ng, A., Rose, S.J., Lewis, C., Riley, D., Gauthier, J.C. & Audebert, P. (2002). Plasma-based studies with intense X-ray and particle beam sources. *Laser Part. Beams* **20**, 527–536.

Linford, G.J., Peressini, E.R., Sooy, W.R. & Spaeth, M.L. (1974). Very long lasers. *Appl. Opt.* **13**, 79–90.

Luther, B.M., Wang, Y., Larotonda, M.A., Alessi, D., Berrill, M., Marconi, M.C., Rocca, J.J. & Shlyaptsev, V.N. (2005). Saturated high-repetition-rate 18.9nm tabletop laser in nickel-like molybdenum. *Opt. Lett.* **30** 165–167.

Mckenna, P., Carroll, D.C., Lundh, O., Nuernberg, F., Markey, K., Bandyopadhyay, S., Batani, D., Evans, R.G., Jafer, R., Kar, S., Neely, D., Pepler, D., Quinn, M.N., Redaelli, R., Roth, M., Wahlstrom, C.-G., Yuan, X.H. & Zepf, M. (2008). Effects of front surface plasma expansion on proton acceleration in ultraintense laser irradiation of foil targets. *Laser Part. Beams* **26**, 591–596.

Nagler, B., Zastrau, U., Fäustlin, R.R., Vinko, S.M., Whitcher, T., Nelson, A.J., Sobierajski, R., Krzywinski, J., Chalupsky, J., Abreu, E., Bajt, S., Bornath, T., Burian, T., Chapman, H., Cihelka, J., Döppner, T., Düsterer, S., Dzelzainis, T., Fajardo, M., Förster, E., Fortmann, C., Galtier, E., Glenzer, S.H., Gode, S., Gregori, G., Hajkova, V., Heimann, P., Juha, L., Jurek, M., Khattak, F.Y., Khorsand, A.R., Klinger, D., Kozlova, M., Laarmann, T., Lee, H.J., Lee, R.W., Meiwes-Broer, K-H., Mercere, P., Murphy, W.J., Przystawik, A., Redmer, R., Reinholz, H., Riley, D., Ropke, G., Rosmej, F., Saksl, K., Schott, R., Thiele, R., Tiggesbäumker, J., Toleikis, S., Tschentscher, T., Uschmann, I., Vollmer, H.J. & Wark, J.S. (2009). Turning solid aluminium transparent by intense soft X-ray photoionization *Nat. Phys.* **5**, 693–696.

National Research Council, Committee on High Energy Density Plasma Physics, Plasma Science. (2003). *High-Energy-Density Physics: The X-Games of Contemporary Science*. Washington, D.C.: National Research Council, Committee on High Energy Density Plasma Physics, Plasma Science.

Neumayer, P., Bock, R., Borneis, S., Brambrink, E., Brand, H., Caird, J., Campbell, E.M., Gaul, E., Goette, S., Haefner, C., Hahn, T., Heuck, H.M., Hoffmann, D.H.H., Javorkova, D., Kluge, H.J., Kuehl, T., Kunzer, S., Merz, T., Onkels, E., Perry, M.D., Reemts, D., Roth, M., Samek, S., Schaumann, G., Schrader, F., Seelig, W., Tauschwitz, A., Thiel, R., Ursescu, D., Wiewior, P., Wittrock, U. & Zielbauer, B. (2005). Status of PHELIX laser and first experiments. *Laser Part. Beams* **23**, 385–389.

Newman, B.E. (1991). XUV free-electron laser-based projection lithography systems. *Proc. SPIE* **1343**, 214.

Patel, P.K., Mackinnon, A.J., Key, M.H., Cowan, T.E., Foord, M.E., Allen, M., Price, D.F., Ruhl, H., Springer, P.T. & Stephens, R. (2003). Isochoric heating of solid-density matter with an ultrafast proton beam. *Phys. Rev. Lett*. **91**, 125004.

Pert, G.J. (1994). Output characteristics of amplified-stimulated-emission lasers. *J. Opt. Soc. Am. B* **11**, 1425–1435.

Roth, M., Alber, I., Bagnoud, V., Brown, C., Clarke, R., Daido, H., Fernandez, J., Flippo, K., Gaillard, S., Gauthier, C., Glenzer, S., Gregori, G., Günther, M., Harres, K., Heathcote, R., Kritcher, A., Kugland, N., LePape, S., Li, B., Makita, M., Mithen, J., Niemann, C., Nürnberg, F., Offermann, D., Otten, A., Pelka, A., Riley, D., Schaumann, D., Schollmeier, M., Schütrumpf, J., Tampo, M., Tauschwitz, A. & Tauschwitz, An. (2009). Proton acceleration experiments and warm dense matter research using high power lasers. *Plasma Phys. Contr. Fusion* **51**, 124039.

Schaumann, G., Schollmeier, M.S., Rodriguez-Prieto, G., Blazevic, A., Brambrink, E., Geissel, M., Korostiy, S., Pirzadeh, P., Roth, M., Rosmej, F.B., Faenov, A.Y., Pikuz, T.A., Tsigutkin, K., Maron, Y., Tahir, NA. & Hoffmann, D.H.H. (2005). High energy heavy ion jets emerging from laser plasma generated by long pulse laser beams from the NHELIX laser system at GSI. *Laser Part. Beams* **23**, 503–512.

Semkat, D., Redmer, R. & Bornath, Th. (2006). Collisional absorption in aluminium. *Phys. Rev. E* **73**, 066406.

Snavely, R.A., Key, M.H., Hatchett, S.P., Cowan, T.E., Roth, M., Phillips, T.W., Stoyer, M.A., Henry, E.A., Sangster, T.C., Singh, M.S., Wilks, S.C., MacKinnon, A., Offenberger, A., Pennington, D.M., Yasuike, K., Langdon, A.B., Lasinski, B.F., Johnson, J., Perry, M.D. & Campbell, E.M. (2000). Intense high-energy proton beams from petawatt-laser irradiation of solids. *Phys. Rev. Lett*. **85**, 2945–2948.

Tommasini, R. & Fill, E.E. (2000). Generalized Linford formula. *J. Opt. Soc. Am. B* **17**, 1665–1670.

Zvorykin, V.D., Didenko, N.V., Ionin, A.A., Kholin, I.V., Konyashchenko, A.V., Krokhin, O.N., Levchenko, A.O., Mavritskii, A.O., Mesyats, G.A., Molchanov, A.G., Rogulev, M.A., Seleznev, L.V., Sinitsyn, D.V., Tenyakov, S.Y., Ustinovskii, N.N. & Zayarnyi, D.A. (2007). GARPUN-MTW: A hybrid Ti : Sapphire/KrF laser facility for simultaneous amplification of subpicosecond/nanosecond pulses relevant to fast-ignition ICF concept. *Laser Part. Beams* **25**, 435–451.